Received 12 September 2025; accepted 15 September 2025. Date of publication 22 September 2025; date of current version 24 November 2025.
Digital Object Identifier 10.1109/OJAP.2025.3612587

Dual-Band and Dual Wide-Angle Scanning Heterogeneous Metasurface-Based Antenna Array in Large Frequency Ratio Integrating With Millimeter-Wave Phased Arrays in Same Aperture

LI WEI[1], WANCHEN YANG[2,3] (Senior Member, IEEE), GUOPING TAN[1] (Senior Member, IEEE), CHUJUN LIANG[3], ZHONGYING WANG[3], AND WENQUAN CHE[3] (Fellow, IEEE)

[1]College of Information Science and Engineering, Hohai University, Nanjing 211100, China
[2]College of Electronic and Information Engineering, Nanjing University of Aeronautics and Astronautics, Nanjing 211106, China
[3]Guangdong Key Laboratory of Millimeter-Waves and Terahertz and the School of Electronic and Information Engineering, South China University of Technology, Guangzhou 510641, China

CORRESPONDING AUTHOR: W. YANG (e-mail: wcyang@nuaa.edu.cn)

This work was supported by the National Natural Science Foundation of China under Grant 62471219 and Grant 62321002.

ABSTRACT The manuscript presents a 4×4 Sub-6GHz heterogeneous metasurface-based array integrated with 8×8 millimeter-wave (mmW) phased array within same aperture. Firstly, two heterogeneous Sub-6GHz antenna elements are designed based on a square ring metasurface (SRMS) and an overlapped metasurface (OLMS), respectively. The SRMS-based antenna is stacked above the 8×8 mmW array without occupying additional space, while the feeding networks of the Sub-6GHz and mmW antennas are also integrated together in one package using the low-temperature-cofired ceramic (LTCC) technology. In addition, the OLMS-based antenna offers the same bandwidth and wider beam than the former. Through near-field analysis of the array, phase differences resulting from the height variation among the heterogeneous elements have been compensated. Secondly, the heterogeneous antennas are constructed to a 4×4 Sub-6GHz array, with two 8×8 mmW arrays integrated beneath the SRMS-based elements. To ensure the scanning performance of the heterogeneous Sub-6GHz array, several dummy metasurface (MS) are loaded at sides to enhance radiation while increasing the scanning angle. Besides, a π-shaped decoupling paths are loaded between adjacent elements, which can cancel the inherent couplings with scanning efficiency increasing. Finally, the proposed heterogeneous array is fabricated and measured. The 4×4 Sub-6GHz heterogeneous array integrating with the mmW arrays can operate in 3.3-3.6GHz and 24.25-29.5GHz. The array can achieve a wide-angle scanning range from –55° to 55° with high isolation of over 20dB in both bands. Compared with other works, it not only realizes aperture-shared integration of Sub-6GHz phased array and mmW phased array, but also ensure dual-band wide-angle scanning, which can be potentially applied in future multi-band base-station antennas.

INDEX TERMS Aperture-shared, heterogeneous antenna, high-isolation, metasurface, wide-angle scanning.

I. INTRODUCTION

As 5G communication technology develops rapidly, an increasing number of frequency bands are being incorporated into 5G systems. There are two main frequency ranges: Sub-6GHz is used for wide coverage, and the mmW is used for high-rate communication. Consequently, more antennas operating in different bands will be integrated into base stations [1]. This integration raises several challenges. On one hand, the multi-band antennas will make the base station crowded while the different-band antennas might interfere with each other. On the other hand, the antennas are required to exhibit wide-angle scanning capability [2], [3] to cover a wider area [4], [5] and increasing channel capacity, etc. Therefore, multi-band aperture-shared antennas with multi-band wide-angle scanning capability are necessary, especially in Sub-6GHz and millimeter wave (mmW) bands.

The aperture-sharing methods for multi-band antennas are mainly two approaches. The traditional approach places different-band antennas close together but with low space utilization. The other method integrates low-frequency (LF) and high-frequency (HF) antennas into the same aperture using a stacked architecture [6]. In this method, the space can be fully utilized, but the interference between the different-band antennas is inevitable. In order to solve this problem, several techniques have been proposed. One approach is to use frequency selective surface (FSS) [7], [8] to construct a pass band to suppress the blockage effect. In addition, from the radar cross section (RCS) perspective [9], a lower RCS can reduce the scattering from the upper antenna, thereby improving the transmission of the underlying antenna. Moreover, the use of filtering structures to suppress parasitic resonances can also maintain the radiation pattern [10], [11]. However, most of these designs are primarily applied to lower-frequency-band antennas (e.g., Sub-6GHz) with limited frequency ratios [12], [13], [14], [15], and they often fail to achieve wide-angle scanning capability coupled with high isolation performance, both of which are critical for 5G applications [16], [17].

When the aperture-shared methods are applied to the integration of Sub-6GHz and mmW antennas, the complexity of the design will be further increased in such large frequency ratio. It is necessary to consider not only the blockage effect between antennas [18], but also the integration challenges of the feeding networks [19]. In [18], the aperture-shared antenna decrease the blockage effect by constructing a perforated patch as the LF antenna. The antenna achieves aperture-shared integration in 7.8-times frequency ratio, but it only scans to ±25° in mmW. In [19], an aperture-shared antenna with Sub-6GHz and mmW integrated feeding network is designed, which can scan to ±45° in mmW. The feeding networks of Sub-6GHz and mmW can work separately without affecting each other under 7.3-times frequency ratio. However, the antenna still remains limited to single-band scanning. Therefore, it is highly significant to research the integration of Sub-6 GHz and mmW arrays, both of which are capable of wide-angle scanning. Utilizing heterogeneous antennas offers a potential solution to overcome these limitations [20].

In this manuscript, a Sub-6GHz antenna array based on heterogeneous metasurface antenna elements is proposed, which can integrate with millimeter-wave (mmW) phased arrays as well as high-integrated dual-band feeding networks. The heterogeneous antennas are based on square ring metasurface (SRMS) and overlapped metasurface (OLMS). The SRMS-based antenna can achieve a high integration with an 8×8 mmW array while the OLMS-based antenna can ensure wide-angle scanning performance of the Sub-6GHz antenna array. Finally, the Sub-6GHz antenna can scan up to ±55° in band with high isolation of larger than 20dB. Moreover, the mmW phased array can also realize wide-angle scanning and high-isolation performance. As results, the proposed aperture-shared architecture can achieve a compact integration of Sub-6GHz array and mmW array. In such architecture, the space utilization of the base station can increase significantly, which has potential advantages in future 5G applications.

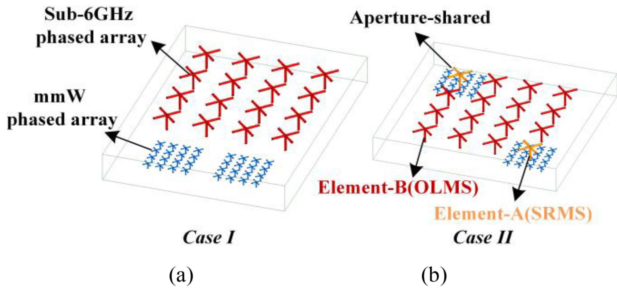

FIGURE 1. The integration architectures: (a) traditional, and (b) aperture-shared architectures.

II. SUB-6GHZ HETEROGENEOUS ANTENNA BASED ON DIVERSIFIED METASURFACE

The traditional aperture-sharing approach places different-band antenna arrays in separate locations, as shown in Fig. 1(a) *Case I*. However, this method requires excessive space, which may not be suitable for crowded base-station applications as future communication systems demand more antennas. One aperture-shared method can improve the space utilization (shown in Fig. 1(b)), where the HF antenna arrays are placed below the LF elements. It is found that the space required by the aperture-shared antenna array in *Case II* decreases significantly without adding extra profile. Therefore, the aperture-shared method that integrates the multi-band antenna into a same aperture can save more space in the applications of multiple antennas.

A. TWO KINDS OF HETEROGENEOUS SUB-6GHZ ANTENNAS

To achieve the aperture-shared architecture, two kinds of heterogeneous Sub-6GHz antennas based on metasurface are proposed. One of the antennas is based on a SRMS [21], which exhibits high transparency to the mmW antenna array, as depicted in Fig. 2(a). For clearly illustrating the Sub-6GHz antenna, the structures of the mmW array have been omitted in 3D view. The SRMS has a hollow part in the middle of the square ring, which exhibits high-transparent performance in mmW. To further improve the transmission, some frequency selective structures (FSS) are loaded near the SRMS. The SRMS is etched on the bottom surface of a slab of Rogers 4003. In addition, it is fed by slot coupling through a stripline by using low temperature-cofired ceramic (LTCC) technology. The Sub-6GHz feeding network is highly integrated with that of the mmW array, as shown in Fig. 2(b). The details of the SRMS-based antenna are

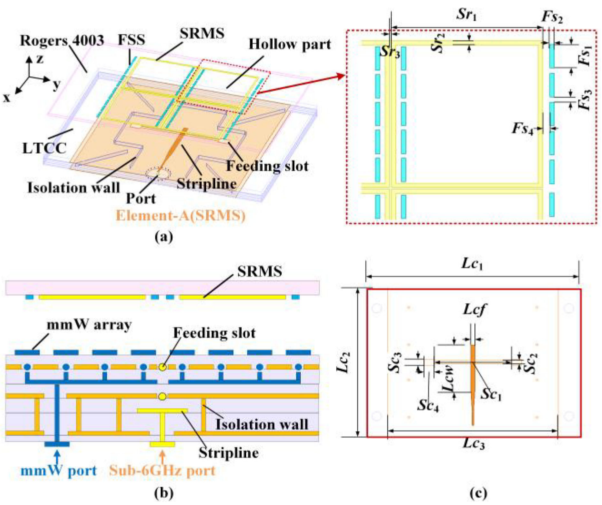

FIGURE 2. The typology of the proposed SRMS-based antenna: (a) 3D view, (b) side view and (c) the details of the structure. (Lc1=50, Lc2=36, Lc3=36, Lcf= 1, Lcw=10.5, Sc1=18.1, Sc2=0.8, Sc3=1.5, Sc4=2.3, Sr1=13.7, Sr2=0.4, Sr3=0.15, Fs1=2.2, Fs2=0.4, Fs3=0.5, Fs4=0.65. Unit: mm).

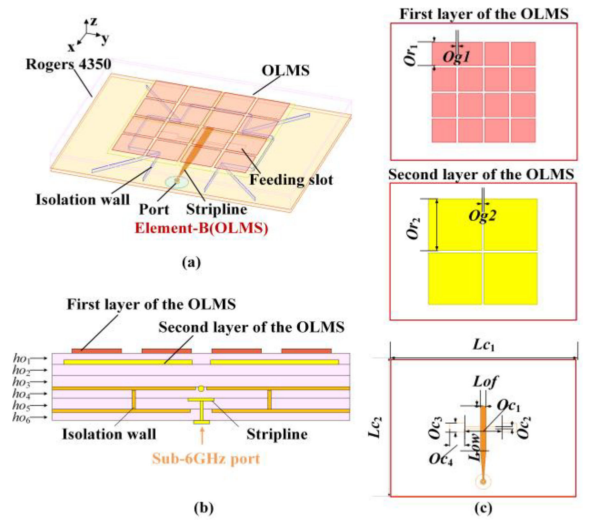

FIGURE 3. The typology of the proposed OLMS-based antenna: (a) 3D view, (b) side view and (c) the details of the structure. (ho_1=0.508, ho_2=1.524, ho_3=1.524, ho_4=0.254, ho_5=0.508, ho_6= 0.254, Or_1=6.7, Or_2=14.4, Og_1=0.6, Og_2=0.6, Oc_1=10, Oc_2=0.6, Oc_3=2.5, Oc_4=4, Low=12.5, Lof=1.5. Unit: mm).

shown in Fig. 2(c). The S-parameters and radiation pattern of the SRMS-based antenna are displayed in Fig. 4, From the results, the SRMS can cover from 3.3 to 3.6 GHz and the 3-dB beamwidth in the E-plane is about 68°.

Another antenna is designed based on OLMS, as shown in Fig. 3(a)(b). The OLMS is constructed by a dual-layer MS, which is etched on the top and bottom of a slab of Rogers 4350, respectively. The OLMS can ensure a broad band while significantly minimizing the size of the antenna [22]. The details of the OLMS-based antenna are shown in Fig. 3(c). From the results in Fig. 4, the OLMS can also cover 3.3-3.6GHz while exhibiting a wider beamwidth in the E-plane of about 90°. Based on the superposition principle of patterns, using an antenna element with wider beam in a phased array can achieve a larger scanning range.

B. DESIGN AND PHASE CENTER ANALYSIS OF 1×4 HETEROGENEOUS ANTENNA ARRAY

When forming an array with heterogeneous elements, their structural differences between them will result in different phase centers. If this discrepancy are not compensated, the overall performance of the antenna array will be affected. To investigate the distinct phase centers arising from the heterogeneous antenna elements, a 1×4 antenna array in line arrangement is used to analyze the phase center distribution. The distance between the phase centers of the adjacent antennas is 38mm along the x-direction (see in Fig. 5). An observed plane is located at the center of the array, and the difference of the phase center can be analyzed using the field calculator in HFSS software. The near-field phase distribution is extracted along a reference line located 0.1λ above the SRMS on the observed plane. The results show that the phase difference between the heterogeneous antennas is approximately 56°. Before phase compensation, the sidelobe of the radiation pattern in the E plane is high, as

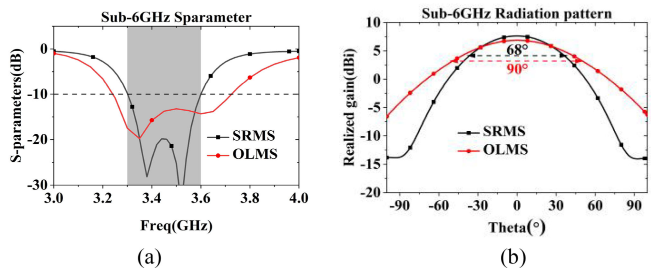

FIGURE 4. The performance of the SRMS-based and OLMS-based antennas: (a) S-parameters and (b) radiation pattern at E-plane.

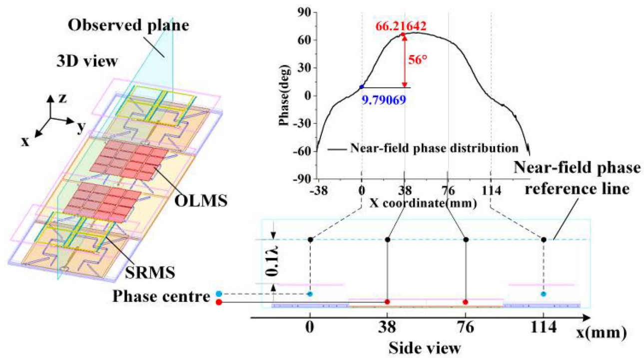

FIGURE 5. The phase centre analysis of the 1×4 heterogeneous array with 3D view, side view and observed plane.

shown in Fig. 6. After compensating for the phase difference by adjusting the port excitations, the radiation pattern is significantly, exhibiting lower sidelobe and higher gain.

III. SUB-6GHZ WIDE-SCANNING PHASED ARRAY BASED ON HETEROGENEOUS ELEMENTS

Based on the above heterogeneous antenna elements, a 4×4 Sub-6GHz wide-scanning phased array is proposed, which is integrated with two 8×8 mmW phased arrays (see Fig. 7).

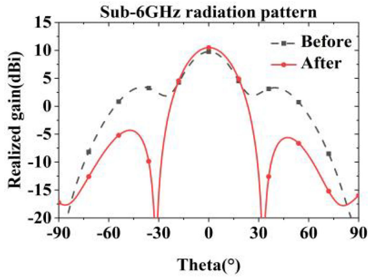

FIGURE 6. Radiation patterns at E plane of the 1×4 heterogeneous array before and after compensating the phase difference of the heterogeneous elements.

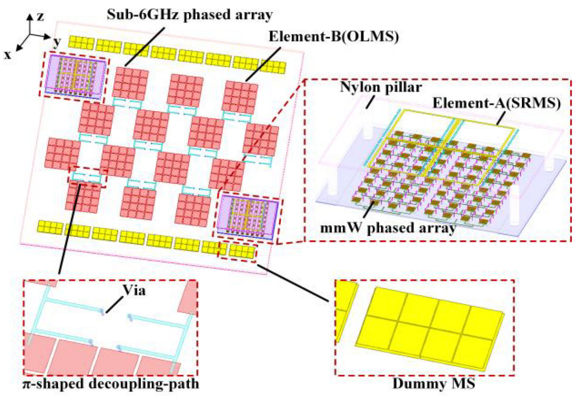

FIGURE 7. The topology of the proposed 4×4 Sub-6GHz wide-scanning phased array integrating with 8×8 mmW phased arrays.

The Sub-6GHz phased array is designed to scan along x-axis, while the elements along y-axis are connected to power dividers. The array is assigned in a triangle arrangement including 14 OLMS-based and 2 SRMS-based elements. The OLMS-based elements have wider beamwidth which helps to extend the scanning range. In addition, each SRMS-based element can compactly integrate with an 8×8 mmW phased array for mmW applications in 5G communication systems. The SRMS is supported by four nylon pillars above the mmW phased array. What's more, in order to further increase the scanning performance of the proposed Sub-6GHz phased array, some dummy MS are placed around the two sides of the array, and several π-shaped decoupling paths are loaded between the adjacent Sub-6GHz elements. This aperture-shared architecture not only realizes a compact integration of the Sub-6GHz and mmW phased arrays with large frequency ratio, but also ensures dual-band wide-angle scanning, which has potential for application in future multi-band base-station. The detailed analysis of the proposed array is provided as follows.

A. 1×4 BEAM-SCANNING SUB-ARRAY BASED ON OLMS ELEMENT WITH DUMMY ELEMENTS

In order to analyze the scanning performance of the Sub-6GHz phased array, here a 1×4 sub-array based on OLMS elements is constructed (see Fig. 8(a)). The sub-array analysis method significantly reduces computational complexity while ensuring accuracy. Because the array performance is mainly determined by OLMS, they are selected for sub-array construction. Note that the length Wd_1 of the ground is slightly larger than that of the four elements for assembly, which may slightly worsen the scanning performance of the array. Here, a dummy MS is introduced to improve the scanning capability. The scanning performance of the *Case I* is indicated by the dashed line in Fig. 9(a), where the largest scanning angle is only ±53°.Therefore, to further improve the scanning performance, a dummy MS is proposed and placed on both sides of the array, along with an additional isolation wall (see Fig. 8(b)). The structure of the dummy MS is clearly shown in Fig. 8(c). It is also constructed using the overlapped MS with a bone-shaped slot on the ground. If a feeding stripline is placed below the slot, the dummy MS can also operate like an antenna in 3.3-3.6GHz, as shown in Fig. 10. Note that the dummy MS is only constructed by half OLMS, so it occupies very little space. The feeding stripline shown in Fig. 10 is not integrated into the array. The dummy MS would be excited by adjacent antenna elements through coupling.

After loading the dummy MS, the phased array can scan up to ±55° in 3.6GHz, as illustrated in Fig. 9(a). To further analyze the mechanism of the dummy MS, Fig. 11 compares the current distributions on the ground before and after loading the dummy MS. Without dummy MS in Fig. 11(a), there are many chaotic currents at the edge of the ground, which would participate in the radiation of the array. After that, the chaotic currents with uncontrollable direction and phase will ultimately affect the scanning performance. It can be clearly observed from Fig. 11(b) that the electric field at the edge of the ground exhibits a weak intensity. However, after loading the dummy MS, the chaotic current is significantly suppressed. Because the dummy MS is coupled from adjacent OLMS-based element, the current direction and phase on the ground beneath the dummy MS agree well with those beneath the OLMS-based element. In addition, as shown in Fig. 11(b), the electric field of the sub-array is enhanced by the dummy MS. Therefore, the dummy MS operates as an expanded element of the array and significantly improves the scanning performance. Fig. 9(b) demonstrates that, after loading the dummy MS, the 1×4 sub-array can scan up to ±55° with a gain decrease less than 3dB.

B. DECOUPLING DESIGN OF TRIANGLE SUB-ARRAY FOR HIGH ISOLATION

As the 4×4 Sub-6GHz antenna array scans only along the *x*-axis, the elements in the same column along *y*-axis are connected to the same power dividers, as shown in Fig. 12. Since the array is assigned in triangle arrangement, it is necessary to analyze the isolation between adjacent sub-arrays. The isolation in triangle-arranged array is a little different from the rectangle-arranged array. Thus, the triangle-arranged array must be divided into multiple triangle sub-arrays to consider the isolation issue. In the triangle sub-array, the *Ant.1* is from the first column is defined as

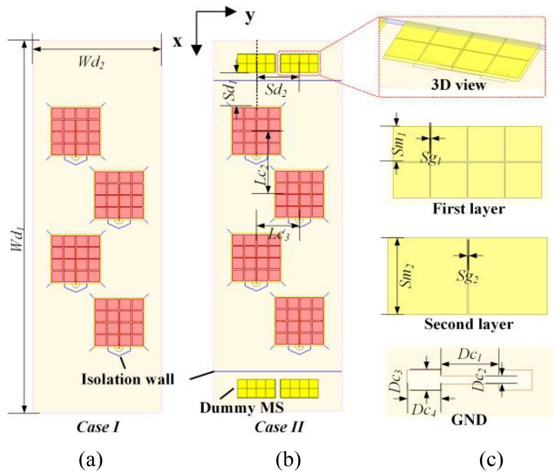

FIGURE 8. The 1×4 sub-array of the Sub-6GHz array based on OLMS element. (a) prototype of the sub-array, (b) the sub-array loading dummy MS and (c) the typology of the dummy MS. (Wd_1=222, Wd_2=75, Sd_1=13.3, Sd_2=25, Lc_2=38, Lc_3=19, Sm_1=5.3, Sm_2=11, Sg_1=0.15,Sg_2=0.15, Dc_1=11, Dc_2=1, Dc_3=2.5 Dc_4=4. Unit: mm).

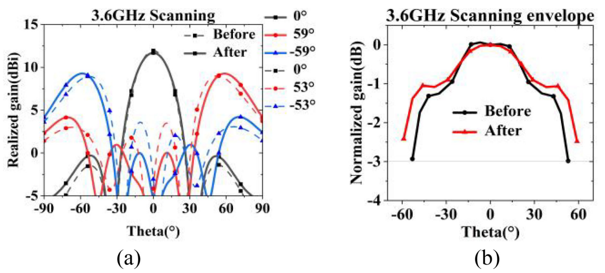

FIGURE 9. The scanning performance of the sub-arraywith or without dummy MS: (a) scanning radiation patterns and (b) scanning envelopes at 3.6GHz.

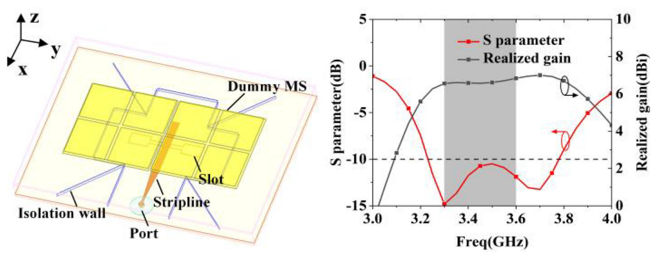

FIGURE 10. The bandwidth of the proposed dummy MS-based antenna.

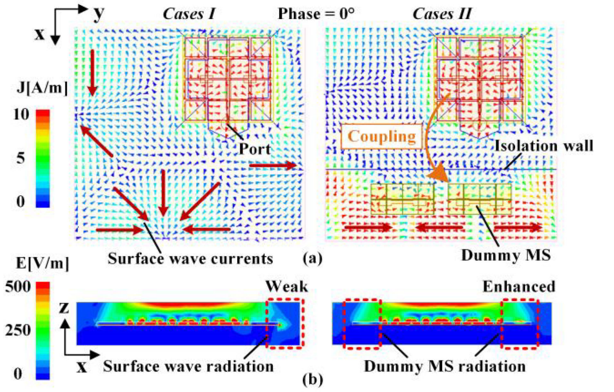

FIGURE 11. The (a) currents on the ground in front view, and (b) the electric field in side view of the sub-array.

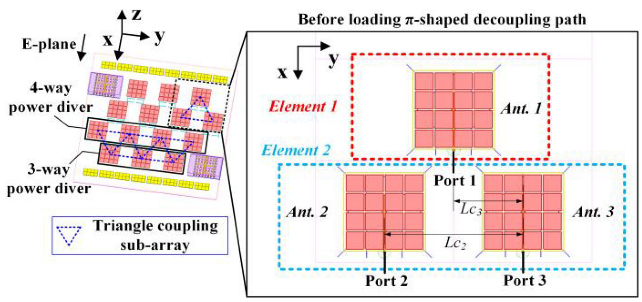

FIGURE 12. The triangle sub-array in the proposed array.

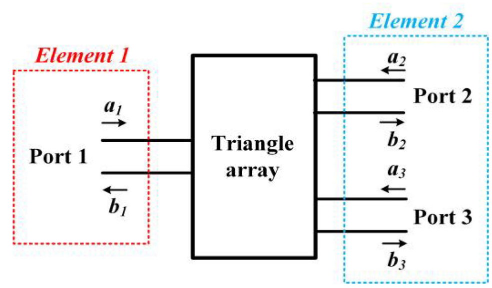

FIGURE 13. The three-port network of the triangle sub-array.

Element1, meanwhile, the group of *Ant.2* and *Ant.3* (defined as *Element2*) from the second column are connected via a power divider and are excited simultaneously. In other words, the triangle sub-array can be treated as a three-port network, with *Element.2* excited by a common-mode signal. Based on the impedance analysis of two-port network, an analysis method of three-port network is employed here.

The three-port network is shown Fig. 13. Parameters a_1, a_2, a_3 represent to the incident waves and the b_1, b_2, b_3 represent to the reflected waves. These waves satisfy the formula (1)

$$\mathbf{B} = \begin{bmatrix} b_1 \\ b_2 \\ b_3 \end{bmatrix} = \begin{bmatrix} S_{11} & S_{12} & S_{13} \\ S_{21} & S_{22} & S_{23} \\ S_{31} & S_{32} & S_{33} \end{bmatrix} \begin{bmatrix} a_1 \\ a_2 \\ a_3 \end{bmatrix} = \mathbf{SA} \quad (1)$$

The three-port network can also be regarded as composing by a single-end port (Port 1) from Element1 and a dual-ended port (Port 2,3) from *Element2* respectively inspired by common-mode and differential-mode signals [23]. Thus, the incident and reflected waves satisfy the following relation:

$$\mathbf{A}' = \begin{bmatrix} a_1 \\ a_{com} \\ a_{dif} \end{bmatrix} = \frac{1}{\sqrt{2}} \begin{bmatrix} \sqrt{2} & 0 & 0 \\ 0 & 1 & 1 \\ 0 & 1 & -1 \end{bmatrix} \begin{bmatrix} a_1 \\ a_2 \\ a_3 \end{bmatrix} = \mathbf{MA} \quad (2)$$

$$\mathbf{B}' = \begin{bmatrix} b_1 \\ b_{com} \\ b_{dif} \end{bmatrix} = \frac{1}{\sqrt{2}} \begin{bmatrix} \sqrt{2} & 0 & 0 \\ 0 & 1 & 1 \\ 0 & 1 & -1 \end{bmatrix} \begin{bmatrix} b_1 \\ b_2 \\ b_3 \end{bmatrix} = \mathbf{MB} \quad (3)$$

$$\mathbf{B}' = \begin{bmatrix} b_1 \\ b_{com} \\ b_{dif} \end{bmatrix} = \begin{bmatrix} S_{11}' & S_{12}' & S_{13}' \\ S_{21}' & S_{22}' & S_{23}' \\ S_{31}' & S_{32}' & S_{33}' \end{bmatrix} \begin{bmatrix} a_1 \\ a_{com} \\ a_{dif} \end{bmatrix} = \mathbf{S}'\mathbf{A}' \quad (4)$$

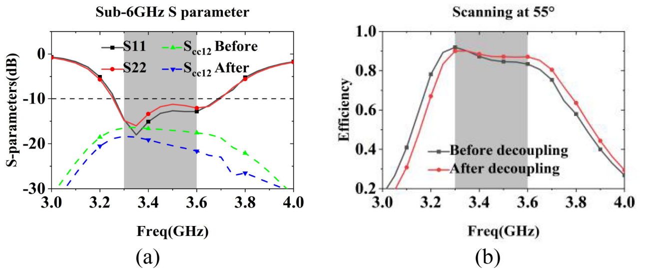

FIGURE 14. The comparisons of the triangle sub-array before and after decoupling. (a) S-parameters and (b) the efficiency scanning at the largest angle.

And then, the matrix can be derived as follows:

$$\mathbf{B}' = \mathbf{MB} = \mathbf{S}'\mathbf{A}' = \mathbf{S}'\mathbf{MA} \tag{5}$$

$$\mathbf{B} = \mathbf{M}^{-1}\mathbf{S}'\mathbf{MA} \tag{6}$$

Comparing with the formula (1) and (6) can calculate that

$$\mathbf{S}' = \mathbf{MSM}^{-1} \tag{7}$$

Finally, after calculating the formula (7), the matrix of the three-port network can be written as formula (8), shown at the bottom of the page, where the common-mode isolation (S_{cc12}) and differential-mode isolation (S_{dd12}) are given by formula (9).

$$S_{cc12} = S_{12}{}' = \frac{1}{\sqrt{2}}(S_{12} + S_{13}) S_{dd12} = S_{13}{}' = \frac{1}{\sqrt{2}}(S_{12} - S_{13}) \tag{9}$$

Using the common-mode isolation (S_{cc12}) to analyze the couplings in triangle sub-array, the results are shown in Fig. 14(a). It can be seen that the common-mode isolation (S_{cc12}) is only about 16dB. To further reduce the coupling, a pair of π-shaped decoupling paths are loaded between the elements [24] within the sub-array (see Fig. 15). Each path consists of a π-shaped stripline and two vias. The stripline is located in the middle layer between the ground and the OLMS, which avoids intersection with the OLMS.

The principle of the decoupling path is shown in Fig. 16. The inherent coupling between the antennas is S_{21C} and the coupling introduced by decoupling path is $S_{21D.}$ When their amplitudes are equal and the phases are opposite, the overall coupling is effectively canceled. From the electric field distribution, the coupling to *Ant.2* is significantly reduced after loading the π-shaped decoupling path. The common-mode isolation of the triangle sub-array is also improved, which is larger than 19.5dB, as shown in Fig. 14(a). In addition, with improved isolation, the efficiency of the triangle sub-array increases by up to 3% when the 4×4 array is scanning at the largest angle, as shown in Fig. 14(b).

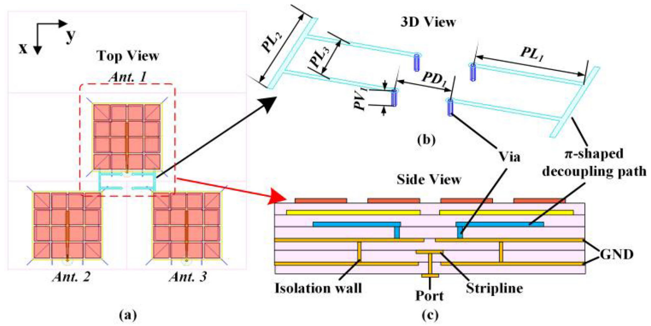

FIGURE 15. The typology of the triangle sub-array after loading π-shaped decoupling path: (a) Top view of the triangle sub-array, (b) 3D view of the π-shaped decoupling path and (c) side view of the triangle sub-array. (PL_1=9.75, PL_2=12, PL_3=6, PD_1=5, PV_1=1.524. Unit: mm).

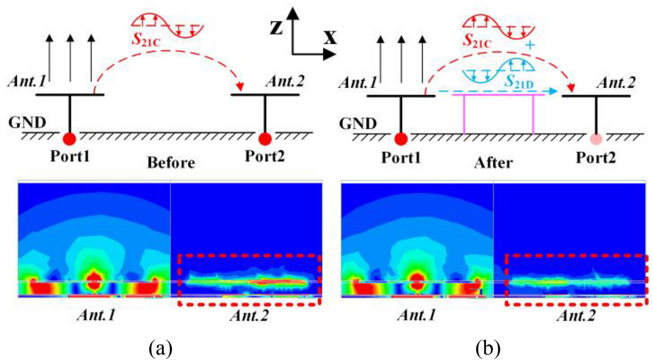

FIGURE 16. The electric field of the triangle sub-array at side view, where only the *Ant.1* is excited:(a) before and (b) after loading the π-shaped decoupling path.

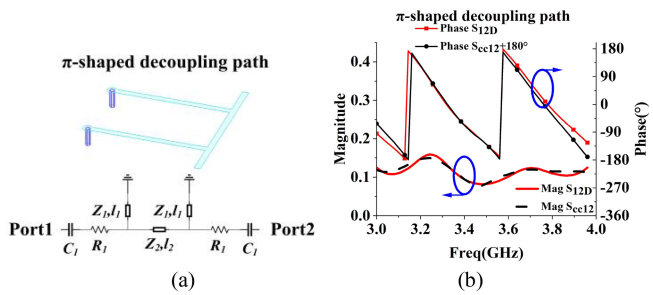

FIGURE 17. The equivalent circuit analysis of the π-shaped decoupling path. (a) equivalent circuit and (b)the comparison of the coupling energy C_1=202fF, R_1=406Ω, Z_1=298Ω, Z_2=200Ω, l_1=48°, l2=240°.

The decoupling path is simulated in ADS (Advanced Design System) using an equivalent circuit (see in Fig. 17), which consists of coupling capacitors, transmission lines and radiation resistors. The transmission line represents the electrical length and impedance of each metal stub in the decoupling path. Since the decoupling path radiates during operation, a radiation resistor is added to represent

$$\mathbf{S}' = \begin{bmatrix} S_{11} & \frac{1}{\sqrt{2}}(S_{12} + S_{13}) & \frac{1}{\sqrt{2}}(S_{12} - S_{13}) \\ \frac{1}{\sqrt{2}}(S_{21} + S_{31}) & \frac{1}{2}(S_{22} + S_{23} + S_{32} + S_{33}) & \frac{1}{2}(S_{22} - S_{23} + S_{32} - S_{33}) \\ \frac{1}{\sqrt{2}}(S_{21} - S_{31}) & \frac{1}{2}(S_{22} + S_{23} - S_{32} - S_{33}) & \frac{1}{2}(S_{22} - S_{23} - S_{32} + S_{33}) \end{bmatrix} \tag{8}$$

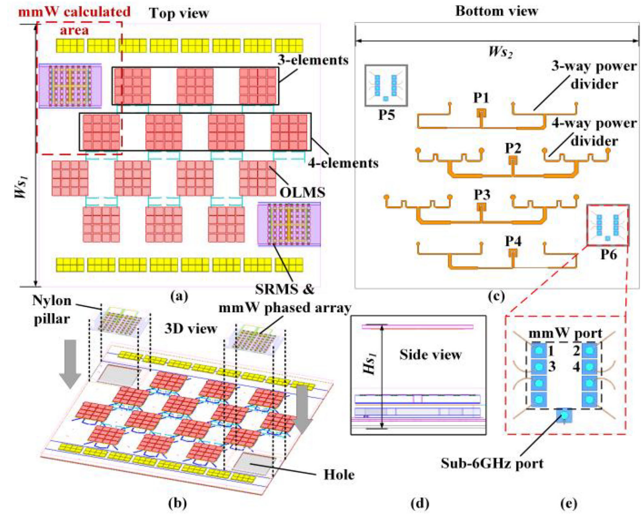

FIGURE 18. The typology of the proposed 4×4 heterogeneous antenna array integrating with 8×8 mmW phased arrays: (a) Top view, (b) 3D view, (c) bottom view, (d) side view of the highest profile and (e) port distribution of the aperture-shared antenna.

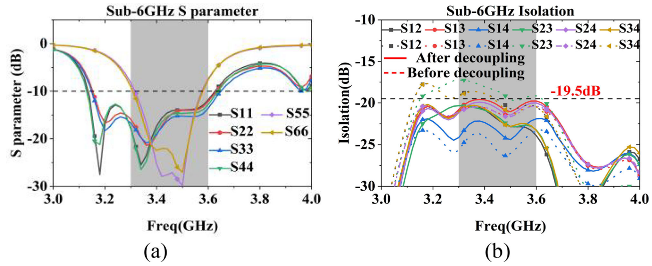

FIGURE 19. The simulated (a) S parameter and (b) isolation of the 4×4 heterogeneous antenna array.

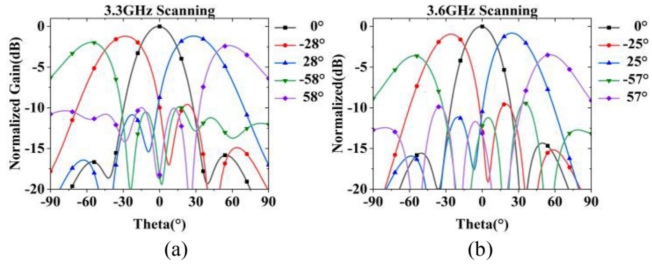

FIGURE 20. The simulated scannning performance at (a) 3.3GHz and (b) 3.6GHz.

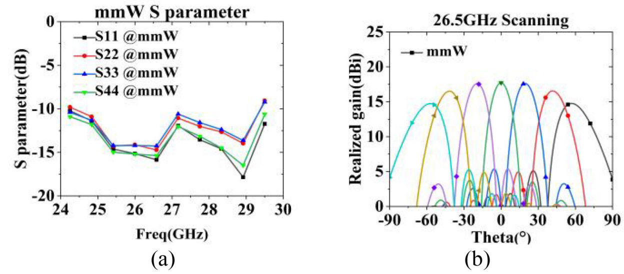

FIGURE 21. Simulated results of the Sub-6GHz & mmW aperture-shared phased array: (a) S parameter and (b) scanning performance at 26.5GHz.

TABLE 1. Simulated performance of the 4×4 heterogeneous antenna array.

Freq (GHz)	Peak gain (dBi)	Scanning range	Scanning gain (dBi)	Gain decrease (dB)
3.3	14.3	±58°	11.95	2.35
3.5	15.62	±56°	12.35	3.27
3.6	15.8	±57°	12.42	3.38
24.25	16.5	±56°	13.88	2.62
26.5	17.44	±56°	14.38	3.06
29.5	17.08	±62°	14.51	2.58

the radiation caused by induced currents. The capacitor represents the coupling between the antenna element and the decoupling path. The coupling coefficient S_{12D} represents the energy transferred from Port 1 to Port 2. Compared with S_{cc12} in the three-port network, S_{12D} exhibits similar magnitude but opposite phase. This demonstrates that the coupling energy introduced by the decoupling path can cancel out the inherent coupling within the three-port network, thus improving isolation between elements.

C. PERFORMANCE OF 4×4 HETEROGENEOUS ANTENNA ARRAY INTEGRATING WITH 8×8 MMW PHASED ARRAYS

Based on the above analyses of wide-angle scanning and high-isolation methods, a 4×4 heterogeneous antenna array integrated with two 8×8 mmW phased arrays is fabricated, as shown in Fig. 18.

The simulation results of the proposed 4×4 heterogeneous antenna array are shown in Figs. 19-21. The results in Fig. 19 indicate that the proposed array cover 3.3-3.6GHz and achieves an isolation of over 19.5dB after loading π-shaped decoupling path. The scanning performance is shown in Fig. 20. It can be seen that, the proposed phased array achieves wide-angle scanning over ±55° across the entire operating band. Furthermore, the performance of the SRMS & mmW aperture-shared phased array in mmW is also provided in Fig. 21. The aperture-shared array can cover 24.25-29.5GHz with large-angle scanning of over ±55°. Note that the simulation of the aperture-shared array considers only the adjacent OLMS and dummy MS (see Fig. 18 mmW calculated area), because the full-array mesh is too large to simulate efficiently. However, the final performance will be validated through measurements and these simulation results serve as a reference. The detailed radiation performance is summarized in Table 1.

IV. MEASUREMENT

For demonstration, the 4×4 heterogeneous antenna array is fabricated, as shown in Fig. 22(a). Four SMA connectors are welded on the feeding networks and the array is assembled using multiple nylon pillars (see Fig. 22(b)). Two SRMS & mmW aperture-shared antennas (named as Ant.A and Ant.B) are integrated with the Sub-6GHz phased array. Each contains an 8×8 mmW phased array, as shown in Fig. 22(c)-(d). The ports of the aperture-shared antenna are welded with SMPM connectors (see Fig. 22(e)).

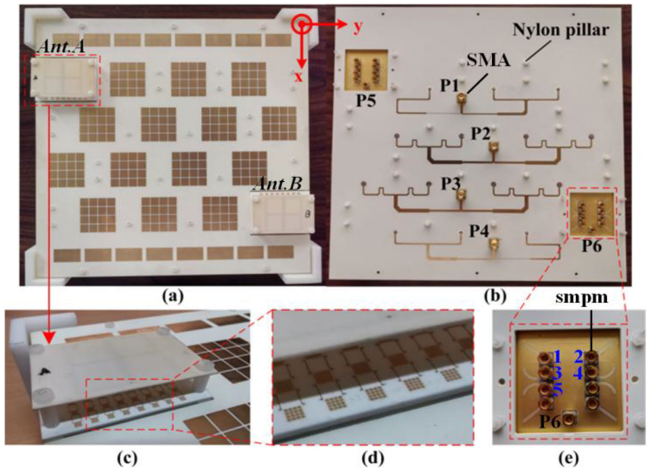

FIGURE 22. The prototype of the fabricated 4×4 heterogeneous antenna array: (a) Top view, (b) bottom view, (c) the SRMS & mmW aperture-shared antenna, (d) the zoom-in view of the 8×8 mmW phased array and (e) port distribution of the aperture-shared antenna.

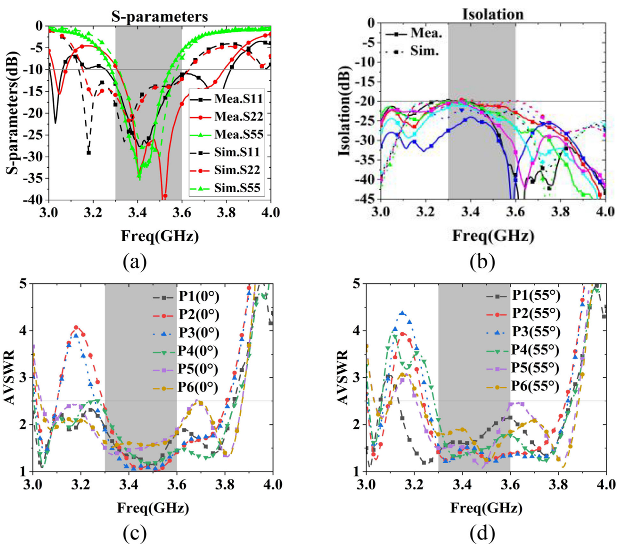

FIGURE 23. Measured results of the 4×4 heterogeneous antenna array in Sub-6GHz. (a) S-parameters, (b) isolation, (c) AVSWR(0°) and (d) AVSWR(55°).

A. MEASURED RESULTS OF THE HETEROGENEOUS SUB-6GHZ ARRAY

The measured Sub-6GHz performance of the phased array are shown in Figs. 23 and 25-26. Fig. 23 presents the S-parameters. The array operates primarily within the 3.3-3.6GHz band. Due to the process error, the bandwidth of the SRMS & mmW aperture-shared array has a slight deviation. Moreover, the measured isolation of the array is larger than 20dB in measurement (see Fig. 23(b)). The AVSWR results in Fig. 23(c-d) show that all ports maintain an AVSWR below 2 under non-scanning conditions. When scanned to the maximum angle, slight performance degradation occurs at some frequencies, but the in-band AVSWR remains below 2.5.

Moreover, the radiation performance was measured using the SATIMO measurement system, as shown in Fig. 24. The measured scanning angle is larger than ±55° across the entire band, closely matching the simulation results (see Fig. 25). Furthermore, the measured gain is approximately 1 dB lower than of the simulation, which can be attributed to fabrication and assembly tolerances.

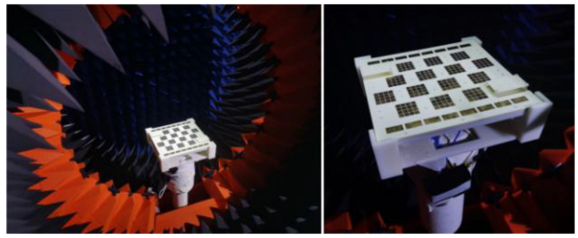

FIGURE 24. The radiation measurements of the proposed 4 × 4 heterogeneous antenna array in Satimo measuring system.

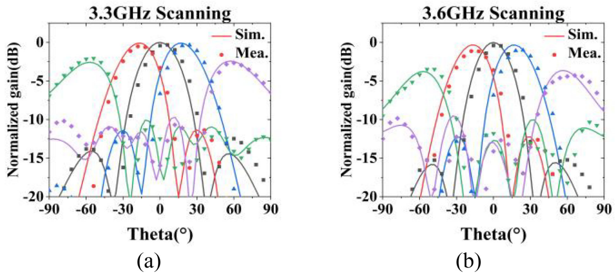

FIGURE 25. Measured scanning performance in E-plane of the 4 × 4 heterogeneous antenna array in Sub-6GHz.

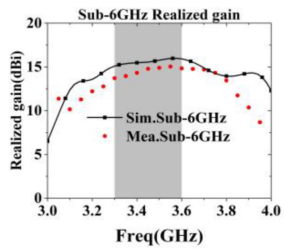

FIGURE 26. Measured realized gain of the 4 × 4 heterogeneous antenna array in Sub-6GHz.

B. MEASURED RESULTS OF THE MMW ARRAY IN THE HETEROGENEOUS SUB-6GHZ ARRAY

In addition, the measured results of the phased array in mmW are also provided. The integrated 8×8 mmW array covers 24.25-29.5GHz with high isolation of mostly larger than 20dB, as shown in Fig. 27. Furthermore, the measured realized gain is a slightly lower than of the simulation. The primary reason is that the mmW phased array is surrounded by the large ground of the Sub-6GHz array, resulting in some scattering currents on the ground that adversely affect mmW radiation. Nevertheless, the gain reduction is mostly within 0.5dB.

From the scanning performance of the mmW array, it can be noted that the performance of the Ant.A and Ant.B exhibits slight variations due to their different positions within the Sub-6GHz array. The detailed measured radiation performance is summarized in Table 2. As shown in Fig. 28, the proposed 4 × 4 heterogeneous antenna array achieves a scanning range of over ±55° in mmW. The radiation pattern

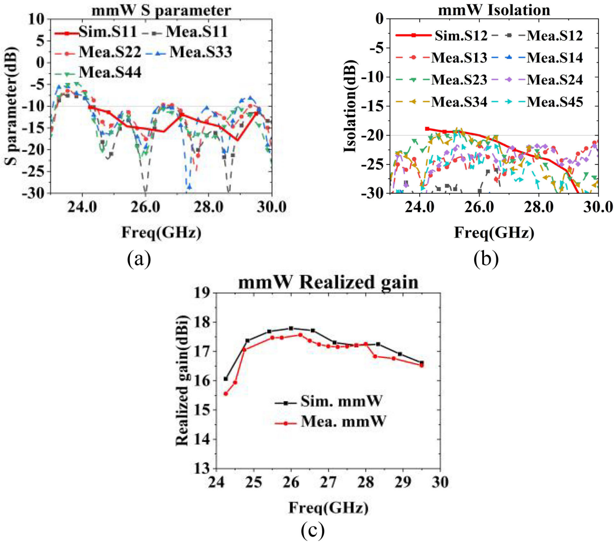

FIGURE 27. Measured results of the 4×4 heterogeneous antenna array in mmW: (a) S parameter, (b) isolation and (c) realized gain.

TABLE 2. Measured scanning performance of the 4×4 heterogeneous array.

Freq (GHz)	Peak gain (dBi)	Scanning range	Scanning gain (dBi)	Gain reduction (dB)
3.3	13.7	±55°	11.67	2.03
3.5	14.8	±56°	12.36	2.44
3.6	14.8	±55°	11.33	3.47
24.25	15.5	±56°	12.86	2.64
26.5	17.3	±56°	15.1	2.2
29.5	16.5	±55°	15.07	1.43

of the Ant.A is slightly deteriorated when scanning close to 60°, which is slightly influenced by the larger ground plane of the Sub-6GHz array. Similarly, the scanning performance of the Ant.B is affected when scanned at –60°. Nevertheless, both antennas achieve a scanning range larger than ±55°.

For further demonstration, comparisons with other previously reported aperture-shared antennas are provided in Table 3. It can be seen that the designs in [14], [15] achieve multi-band aperture sharing through a vertically stacked architecture with wide-angle scanning capability. However, these works employ identical antenna element types within the same frequency band and primarily focus on integration within the Sub-6GHz range. To meet the requirements of 5G applications, the integration of the Sub-6GHz and mmW antennas requires further research. In [18], an aperture-shared antenna achieved the integration of a Sub-6GHz antenna and an mmW phased array. However, it could only scan up to ±25° in mmW. In [19], an aperture-shared antenna achieved a scanning range greater than ±45° in mmW, but it did not support scanning in the Sub-6GHz band. Actually, when the frequency ratio is larger than 4, it is necessary to first consider the aperture-shared integration of the LF element and the HF array, and then achieve the integration of LF and HF array, which is very difficult to simultaneously ensure dual-band scanning performances. However, the proposed 4×4 heterogeneous array successfully achieves effective integration of the Sub-6GHz array and mmW array with better performance. It can scan larger than ±55° in both bands, while maintaining in-band isolation greater than 20dB. In addition, the Sub-6GHz and mmW feeding networks are highly integrated within a single package using LTCC technology, resulting in a more compact aperture-shared antenna design.

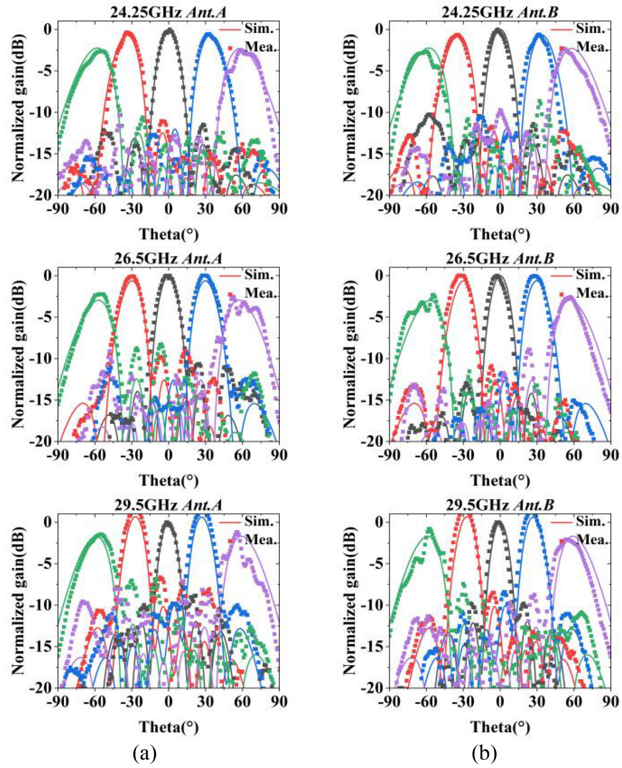

FIGURE 28. The measured scanning performance at E-plane of the 4×4 heterogeneous antenna array in mmW.

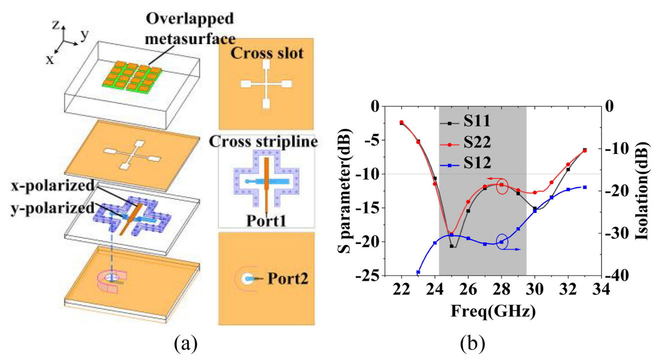

FIGURE 29. Dual-polarized antenna based on overlapped metasurface. (a) 3D view, (b) S parameter and isolation performance.

V. DISCUSSION

Since dual-polarized antennas are widely applied, this section discusses the application of the proposed aperture-shared antenna architecture in dual-polarized scenarios. Because the symmetry of the metasurface, the overlapped metasurface antenna can be designed as a dual-polarized antenna fed by

TABLE 3. Performance comparisons with other reported aperture-shared antennas.

	Antenna Type	Frequency (GHz)	Freq ratio	Aperture-shared method	Scanning range	Dual-band wide scanning
[14]	Dipole element	0.82-1.0 (19.7%)	1:2.2	choked radiator	N.A.	No
	2×2 dipole array	1.71-2.28 (28.5%)			N.A.	
[15]	Dipole element	0.79-0.96 (19.4%)	1:2.2:4	choked radiator	N.A.	No
	2×2 dipole array	1.71-2.17 (23.7%)			N.A.	
	4×8 dipole array	3.4-3.6 (5.7%)			-50° ~ +50°	
[18]	Patch antenna element	3.27-3.71 (11.7%)	1:7.8	structural reuse	N.A.	No
	2×4 DRA	24.4-28 (11.9%)			-25° ~ +25°	
[19]	Patch antenna element	3.45-3.58 (3.7%)	1:7.3	partially reflective surface	N.A.	No
	8×8 patch array	24.5-27 (9.7%)			-45° ~ +45°	
Our work	**4×4 Heterogeneous metasurface array**	**3.3-3.55 (7.2%)**	**1:7.8**	**diversified metasurface**	**-55° ~ +55° (whole band)**	**Yes**
	8×8 metasurface array	**24.25-29.5 (19.5%)**			**-55° ~ +55° (whole band)**	

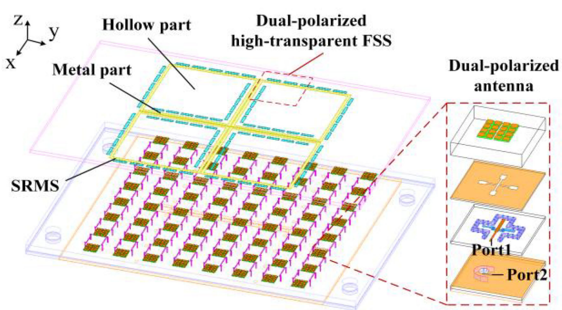

FIGURE 30. aperture-shared antenna in dual-polarized architecture.

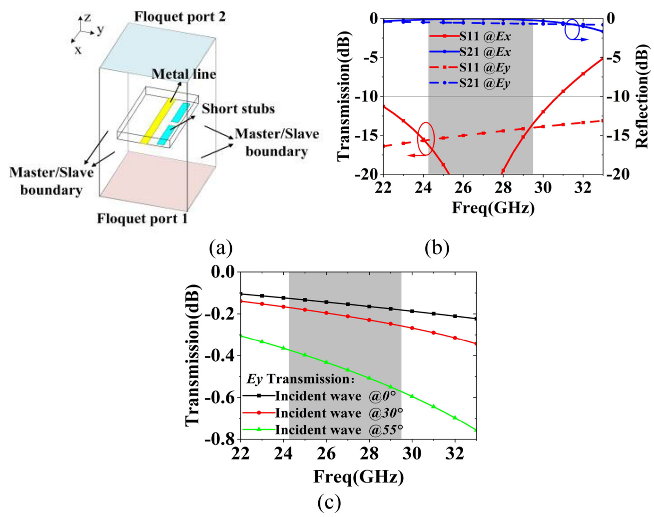

FIGURE 31. Transmission analysis of Ex and Ey. (a) Floquet mode analysis, (b) transmission & reflection coefficients, and (c) transmission of incident wave in different directions.

a cross slot. Here a mmW antenna is used as an example, shown in Fig. 29 (a). In addition, the isolation can achieve larger than 25dB in band, seen in Fig. 29 (b). The SRMS in Sub-6GHz is also symmetric, so it can also be designed as a dual-polarized antenna.

The architecture of the dual-polarized aperture-shared antenna is shown in Fig. 30. A dual-polarized electromagnetically transparent (EM-transparent) structure is analyzed here. The dual-polarized antenna array is placed below a SRMS with dual-polarized EM-transparent FSS. The hollow part of the SRMS has significantly increased the transmission of the Ex- and Ey-polarized waves.

The transmission analysis of Ex and Ey are shown in Fig. 31. The Floquet mode analysis is shown in Fig. 31(a). The results indicate that the proposed FSS structure exhibits a EM-transparent performance for Ey polarization, as shown in Fig. 31(b). In addition, the transmissions of the waves coming different direction are also been discussed in Fig. 31(c). It can be seem that, the transmission of Ey is greater than -0.6dB, which ensures the scanning performance even at large scanning angles.

In summary, due to the dual-polarization capability of the antenna and the FSS, the aperture-shared method proposed in this work can be potentially applied in dual-polarized aperture-shared antenna systems.

VI. CONCLUSION

In this work, a 4×4 Sub-6GHz heterogeneous array integrated with 8×8 mmW arrays is proposed. Firstly, two types of heterogeneous antennas that SRMS-based and OLMS-based antennas are proposed. And then, the heterogeneous antennas are constructed to a 4×4 array in triangle arrangement while integrated with 8×8 mmW array. The antenna arrays achieves dual-band wide-angle scannings and high-isolation performance. Therefore, the proposed 4×4 heterogeneous array integrated with 8×8 mmW arrays exhibits potential application in 5G communication systems.

REFERENCES

[1] J. Li, W. Yang, S. Ma, Q. Xue, and W. Che, "Reconfigurable millimeter-wave tri-band antenna based on VO2-films-embedded co-aperture metasurface structures," *IEEE Trans. Antennas Propag.*, vol. 71, no. 4, pp. 3134–3145, Apr. 2023.

[2] Z.-L. Su, K. W. Leung, and K. Lu, "A shaped-beam antenna for wide-angle scanning phased array," *IEEE Trans. Antennas Propag.*, vol. 70, no. 9, pp. 7659–7669, Sep. 2022.

[3] Z. Wang, S. Zhao, and Y. Dong, "Metamaterial-based wide-beam dielectric resonator antenna for broadband wide-angle beam-scanning phased array applications," *IEEE Trans. Antennas Propag.*, vol. 70, no. 10, pp. 9061–9072, Oct. 2022.

[4] H. Wang, S.-W. Qu, S. Yang, and J. Hu, "Low-profile planar ultrawideband modular antenna array loaded with parasitic metal strips," *IEEE Trans. Antennas Propag.*, vol. 71, no. 7, pp. 5805–5816, Jul. 2023.

[5] S. Yan et al., "A high-isolation high-gain MIMO millimeter-wave antenna array," *IEEE Trans. Antennas Propag.*, vol. 72, no. 2, pp. 1201–1211, Feb. 2024.

[6] Y. Li and Q.-X. Chu, "Shared-radiator design of dual-band coplanar base station antenna array using cavity-backed slots," *IEEE Trans. Antennas Propag.*, vol. 69, no. 12, pp. 8985–8990, Dec. 2021.

[7] P. Mei, S. Zhang, and G. F. Pedersen, "A dual-polarized and high-gain X-/Ka-band shared-aperture antenna with high aperture reuse efficiency," *IEEE Trans. Antennas Propag.*, vol. 69, no. 3, pp. 1334–1344, Mar. 2021.

[8] W. Niu, B. Sun, G. Zhou, and Z. Lan, "Dual-band aperture shared antenna array with decreased radiation pattern distortion," *IEEE Trans. Antennas Propag.*, vol. 70, no. 7, pp. 6048–6053, Jul. 2022.

[9] S. J. Yang, Y. Yang, and X. Y. Zhang, "Low scattering element-based aperture-shared array for multiband base stations," *IEEE Trans. Antennas Propag.*, vol. 69, no. 12, pp. 8315–8324, Dec. 2021.

[10] D. Zhang and Q. Wu, "A shared-aperture antenna with high-aperture reuse efficiency and high isolation based on the Quasi-Yagi structure," *IEEE Trans. Antennas Propag.*, vol. 71, no. 11, pp. 8504–8513, Nov. 2023.

[11] S. J. Yang, W. Duan, Y. Y. Liu, H. Ye, H. Yang, and X. Y. Zhang, "Compact dual-band base-station antenna using filtering elements," *IEEE Trans. Antennas Propag.*, vol. 70, no. 8, pp. 7106–7111, Aug. 2022.

[12] X. Lu, Y. Chen, S. Guo, and S. Yang, "An electromagnetic-transparent cascade comb dipole antenna for multi-band shared-aperture base station antenna array," *IEEE Trans. Antennas Propag.*, vol. 70, no. 4, pp. 2750–2759, Apr. 2022.

[13] D. He, Y. Chen, and S. Yang, "A low-profile triple-band shared-aperture antenna array for 5G base station applications," *IEEE Trans. Antennas Propag.*, vol. 70, no. 4, pp. 2732–2739, Apr. 2022.

[14] H.-H. Sun, C. Ding, H. Zhu, B. Jones, and Y. J. Guo, "Suppression of cross-band scattering in multiband antenna arrays," *IEEE Trans. Antennas Propag.*, vol. 67, no. 4, pp. 2379–2389, Apr. 2019.

[15] Y.-L. Chang and Q.-X. Chu, "Suppression of cross-band coupling interference in tri-band shared-aperture base station antenna," *IEEE Trans. Antennas Propag.*, vol. 70, no. 6, pp. 4200–4214, Jun. 2022.

[16] Y. Sun, J. Zhang, P. Mei, S. Luo, W. Fu, and S. Zhang, "Tri-band dual-polarized shared-aperture antenna arrays with wide-angle scanning and low profile for 5G base stations," *IEEE Trans. Antennas Propag.*, vol. 72, no. 3, pp. 2455–2467, Mar. 2024.

[17] C. X. Bai, Y. J. Cheng, Y. R. Ding, and J. F. Zhang, "A metamaterial-based S/X -band shared-aperture phased-array antenna with wide beam scanning coverage," *IEEE Trans. Antennas Propag.*, vol. 68, no. 6, pp. 4283–4292, Jun. 2020.

[18] X.-H. Ding, W.-W. Yang, W. Qin, and J.-X. Chen, "A broadside shared aperture antenna for (3.5, 26) GHz mobile terminals with steerable beam in millimeter-waveband," *IEEE Trans. Antennas Propag.*, vol. 70, no. 3, pp. 1806–1815, Mar. 2022.

[19] L. Wen et al., "A dual-polarized aperture-sharing phased-array antenna for 5G (3.5, 26) GHz communication," *IEEE Trans. Antennas Propag.*, vol. 71, no. 5, pp. 3785–3796, May 2023.

[20] L. Li, S. Liao, W. Che, and Q. Xue, "Wideband wide-angle scanning endfire phased array antenna based on heterogeneous beam elements for millimeter-wave mobile terminals," *IEEE Trans. Antennas Propag.*, vol. 72, no. 2, pp. 1275–1285, Feb. 2024.

[21] L. Wei, W. Yang, Q. Xue, and W. Che, "Aperture-shared design of millimeter-wave phased array and sub-6 GHz antenna using diversified metasurface structures," *IEEE Trans. Antennas Propag.*, vol. 72, no. 8, pp. 6362–6373, Aug. 2024.

[22] D. Chen, W. Yang, W. Che, and Q. Xue, "Miniaturized wideband metasurface antennas using cross-layer capacitive loading," *IEEE Antennas Wireless Propag. Lett.*, vol. 21, pp. 19–23, 2022.

[23] D. E. Bockelman and W. R. Eisenstadt, "Combined differential and common-mode scattering parameters: Theory and simulation," *IEEE Trans. Microw. Theory Techn.*, vol. 43, no. 7, pp. 1530–1539, Jul. 1995.

[24] L. Gu, W. Yang, S. Liao, Q. Xue, and W. Che, "Novel coupling cancellation method by loading planar path for wideband high-isolation wide-scanning millimeter-wave phased array," *IEEE Trans. Antennas Propag.*, vol. 70, no. 11, pp. 10520–10530, Nov. 2022.

LI WEI was born in Huizhou, Guangdong, China, in 1998. He received the B.S. degree in electronic science and technology from Shenzhen University, Shenzhen, China, in 2020, and the M.S. degree in communication engineering from the South China University of Technology, Guangzhou, China, in 2023. He is currently pursuing the Ph.D. degree with Hohai University, Nanjing, China. His current research interests include metasurface antennas, phased array antennas, and aperture-shared antennas based on diversified metasurface structures.

WANCHEN YANG (Senior Member, IEEE) received the B.Eng. degree in communication engineering from Hohai University (HHU), Nanjing, China, in 2010, and the Ph.D. degree in electromagnetic field and microwave technology from the Nanjing University of Science and Technology (NUST), Nanjing, in 2015. From November 2013 to April 2014, she was a Research Assistant with the University of Macau. From May 2017 to November 2017, she was a Postdoctoral Fellow with The City University of Hong Kong. From October 2015 to December 2018, she was an Assistant Professor with NUST. From January 2019 to June 2022, she was an Associate Professor with the South China University of Technology, Guangzhou, China. From July 2022 to July 2024, she was a Professor with HHU. In August 2024, she joined the Nanjing University of Aeronautics and Astronautics, Nanjing, where she is currently a Professor. She has authored or co-authored over 150 internationally refereed journal and conference papers, including over 40 Transaction papers. Her main research interests include novel artificial material-based antenna arrays, multi-functional antenna arrays, millimeter-wave antenna arrays, and MIMO antenna arrays and technologies. She was the recipient of the 2017 Outstanding Doctoral Dissertation of Jiangsu province, China, and the Best Paper Prize of 2014 Student Paper Competition in IEEE HK AP/MTT Postgraduate Conference, October 2014, and the co-recipient of the Best Paper Prize of 2015 Asia Pacific Microwave Conference, December 2015, and the Best Paper Prize of 2022 International Wireless Symposium, August 2022. She serves as an Associate Editor of the *Microwave and Optical Technology Letters* and IEEE ACCESS, and a reviewer of the IEEE TRANSACTIONS ON ANTENNAS AND PROPAGATION, the IEEE TRANSACTIONS ON MICROWAVE THEORY AND TECHNIQUES, the IEEE TRANSACTIONS ON INDUSTRIAL ELECTRONICS, the IEEE ANTENNAS AND WIRELESS PROPAGATION LETTERS, the IEEE ACCESS, the *IET Microwaves Antennas and Propagation*, the *IET Electronic Letters*, and the *Journal of Electromagnetic Waves and Applications*.

GUOPING TAN (Senior Member, IEEE) received the Ph.D. degree in computer science from Saarland University, Germany, in 2009. He is currently a Full Professor with the College of Computer and Software Engineering, Hohai University, Nanjing, China. From 2003 to 2005, he was a Ph.D. student with the National Mobile Communication Research Laboratory, Southeast University, Nanjing. From 2005 to 2009, he was a Researcher with the Telecommunications Laboratory, Saarland University, under DAAD Scholarship. He was a Senior Engineer with ZTE Corporation China from 2000 to 2003, where he was mainly involved in research and development of wireless communication protocols for the base station of CDMA systems. His current research interests mainly include wireless federated learning, mobile-edge AI, and Internet of Vehicles.

CHUJUN LIANG was born in Hubei, China, in 1999. She received the B.Eng. degree in optoelectronics information science and engineering, and the M.Eng. degree in information and communication engineering from the South China University of Technology, Guangzhou, China, in 2021 and 2024, respectively. Her current research interests include metasurface antennas, circularly polarized antennas, base station antennas, beamforming techniques, and wide-angle scanning phased arrays.

ZHONGYING WANG was born in Guangzhou, Guangdong, China, in 1999. He received the B.S. and M.S. degrees in communication engineering from the South China University of Technology, Guangzhou, in 2021 and 2024. He currently serves as a Network Engineer with China Unicom, Guangzhou. He also serves as a Research Assistant with the South China University of Technology. His current research interests include metasurface antennas, wide-beam antennas, beamforming techniques, and wide-angle scanning phased arrays.

WENQUAN CHE (Fellow, IEEE) received the B.Sc. degree from the East China Institute of Science and Technology, Nanjing, China, in 1990, the M.Sc. degree from the Nanjing University of Science and Technology (NUST), Nanjing, in 1995, and the Ph.D. degree from The City University of Hong Kong, Hong Kong, in 2003. In 1999, she joined The City University of Hong Kong, as a Research Assistant, where she was a Research Fellow and a Visiting Professor from 2005 to 2006 and 2009 to 2011. In 2002, she joined the Polytechnique Montréal, Montréal, QC, Canada, as a Visiting Scholar. From 2007 to 2008, she was with the Institute of High Frequency Technology, Technische Universität München, Munich, Germany. From 2008 to October 2018, she was a Professor with NUST. In November 2018, she joined the South China University of Technology, Guangzhou, China, where she is currently a Professor. She has authored or co-authored over 300 internationally referred journal papers and international conference papers. Her research interests include electromagnetic computation, planar/coplanar circuits and subsystems in RF/microwave frequency, microwave monolithic integrated circuits, and medical application of microwave technology.

Dr. Che was the recipient of the 2007 Humboldt Research Fellowship presented by the Alexander von Humboldt Foundation of Germany, the 5th China Young Female Scientists Award in 2008, and the recipient of Distinguished Young Scientist awarded by the National Natural Science Foundation Committee of China in 2012. She is the Editor-in-Chief of the *Microwave and Optical Technology Letters*, a member of IEEE MTT-S AdCom Committee from 2018 to 2020, the Associate Editor of the IEEE Journal of Electromagnetics, RF, and *Microwaves in Medicine and Biology*, and a reviewer for the IEEE Transactions on Microwave Theory and Techniques, the IEEE Transactions on Antennas and Propagation, the IEEE Transactions on Industrial Electronics, and the IEEE Microwave and Wireless Components Letters.